Robust LFC in a Smart Grid With Wind Power Penetration by Coordinated V2G Control and Frequency Controller

Sitthidet Vachirasricirikul and Issarachai Ngamroo, *Member, IEEE*

***Abstract*—In the smart grid, the large scale wind power penetration tends to expand vastly. Nevertheless, due to the intermittent power generation from wind, this may cause a problem of large frequency fluctuation when the load-frequency control (LFC) capacity is not enough to compensate the unbalance of generation and load demand. Also, in the future transport sector, the plug-in hybrid electric vehicle (PHEV) is widely expected for driving in the customer side. Generally, the power of PHEV is charged by plugging into the home outlets as the dispersed battery energy storages. Therefore, the vehicle-to-grid (V2G) power control can be applied to compensate for the inadequate LFC capacity. This paper focuses on the new coordinated V2G control and conventional frequency controller for robust LFC in the smart grid with large wind farms. The battery state-of-charge (SOC) is controlled by the optimized SOC deviation control. The structure of frequency controller is a proportional integral (PI) with a single input. To enhance the robust performance and robust stability against the system uncertainties, the PI controller parameters and the SOC deviation are optimized simultaneously by the particle swarm optimization based on the fixed structure mixed H_2/H_∞ control. Simulation results show the superior robustness and control effect of the proposed coordinated controllers over the compared controllers.**

***Index Terms*—Battery state-of-charge, mixed H_2/H_∞ control, particle swarm optimization, plug-in hybrid electric vehicle, smart grid, vehicle-to-grid.**

NOMENCLATURE

AR	Area requirement.
LFC	Load-frequency control.
PHEV	Plug-in hybrid electric vehicle.
PSO	Particle swarm optimization.
SOC	State-of-charge.
V1G	One-way charge.
V2G	Vehicle-to-grid.
D_1, D_2	Load damping coefficient in area 1 and area 2.
M_1, M_2	Inertia constant in area 1 and area 2.
P_{max}	Maximum V2G power output.
P_{V2G}	V2G power output.
$\Delta f_1, \Delta f_2$	Change of system frequency in area 1 and area 2.
ΔP_{21}	Change of tie-line power flow from area 2 to area 1.
$\Delta P_{AR1}, \Delta P_{AR2}$	Change of AR in area 1 and area 2.
$\Delta P_{th1}, \Delta P_{th2}$	Change of power output of thermal power plant in area 1 and area 2.
$\Delta P_{V2G\_1}, \Delta P_{V2G\_2}$	Change of V2G power in area 1 and area 2.

Manuscript received November 24, 2012; revised March 20, 2013; accepted May 12, 2013. Date of current version December 24, 2013. This work was supported by the King Mongkut's Institute of Technology Ladkrabang Research Fund. Paper no. TSG-00814-2012.

S. Vachirasricirikul is with the Department of Electrical Engineering, School of Engineering, University of Phayao, Phayao 56000 Thailand (e-mail: sitthidetv@hotmail.com; sitthidet.va@up.ac.th).

I. Ngamroo is with the Center of Excellence for Innovative Energy Systems, School of Electrical Engineering, Faculty of Engineering, King Mongkut's Institute of Technology Ladkrabang, Bangkok 10520, Thailand (e-mail: ngamroo@gmail.com).

Color versions of one or more of the figures in this paper are available online at http://ieeexplore.ieee.org.

Digital Object Identifier 10.1109/TSG.2013.2264921

I. INTRODUCTION

CURRENTLY, THE widespread penetration of large scale wind power has been increasing largely because of plentiful availability and reduced CO_2 emissions [1]–[3]. However, the wind power is intermittent in nature. This may cause an imbalance of supply and load demand and lead to a severe frequency oscillation problem [4]. Particularly, this problem may occur considerably when the capacity of LFC is insufficient during the night period [5].

On the other hand, in the future transportation system, the PHEVs are used extensively for driving in the customer side because of low-cost charging, reduced petroleum usages and reduced greenhouse emissions [6]–[8]. For example, as in the U.S. Department of Energy projects, approximately 1 million PHEVs will be on the road by 2015 and 425 000 PHEVs will be sold in 2015 [9]. Also, in China, it is approximated that by 2050 the number of electric cars will reach 200 million for driving [10]. Moreover, there are upward trends to install the PHEVs as the controllable loads in the future smart grid [11], [12]. Mainly, the power of PHEV is charged in the night period owing to the cheap electricity price [13]. Therefore, the V2G power control can be applied to compensate for the LFC capacity in the nighttime [14]. Reference [15] proposes an autonomous distributed V2G control of grid-connected PHEV and EV to the actual frequency measurements in Eastern 50 Hz system and Western 60 Hz system of Japan. In [16], the V2G control based on the

average battery SOC deviation control is applied to compensate the LFC capacity in the system. Reference [17] concentrates on the autonomous distributed V2G control considering the charging request and battery condition for suppressing the fluctuations of frequency and tie-line power flow in the two-area interconnected power system. The battery SOC is controlled by the SOC balance method. In addition, the smart charging control technique is proposed for satisfying the scheduled charging by the vehicle user [18].

However, the V2G control and frequency controller parameters in [17], [18] are separately determined for each area. Hence, they cannot guarantee the well coordinated control effects of V2G and frequency controllers. Moreover, these research works does not take both robust performance and robust stability of the designed controller against system disturbances and uncertainties such as various system operating conditions, unpredictable wind power patterns, and system parameters variation, etc., into account in the design problem. Accordingly, the performance and robustness of designed controllers cannot be guaranteed. The controllers with the high performance and robustness are greatly expected for LFC in the smart power grid.

In order to enhance both performance and robustness of the designed controllers, the conventional mixed H_2/H_∞ controller has been presented in [19], [20]. By optimizing the H_2 and H_∞ norms, the robust performance and robust stability margin can be improved. Nevertheless, the resulted H_2/H_∞ controller still has a high order [19], [20]. As a result, it is difficult to implement in actual power systems. Generally, the controller structures such as lead-lag compensator, and proportional integral (PI) etc., are preferred in practice because of their simple structure and low order [21].

To overcome above problems, this paper proposes the new coordinated V2G control and conventional frequency controller for robust LFC in an interconnected power system with large wind farms. The battery SOC is managed by controlling the optimized SOC deviation based on the balanced SOC control. System uncertainties are formulated by the multiplicative uncertainty [22]. The structure of frequency controller is a PI compensator. The PI parameters are tuned by the PSO [23] based on the fixed-structure mixed H_2/H_∞ control. Simulation studies exhibit the superior robustness and coordinated control effects of the proposed V2G control and PI controllers in comparison to the V2G control and PI controllers in [17], [18] and the V1G control and PI controllers.

II. System Modeling

Fig. 1 shows a smart multi-area interconnected power system with large wind power penetration. The V2G-based PHEVs is applied to compensate the unequal real power in each area when the LFC capacity is not enough. Here, a two-area interconnected power system with large wind farms and PHEVs is considered for the simulation study. With the studied system, each area consists of the wind power, thermal power plant, LFC, PHEV, and load. In area 1, the power capacities of the wind power, thermal power plant, LFC, PHEV, and load are 3600 MW, 24252 MW, 496 MW, 500 MW, and 33090 MW, respectively. Also, the power capacities of the wind power, thermal power plant, LFC, PHEV, and load in area 2 are 3000 MW, 5560 MW, 106 MW, 500 MW, and 7090 MW, respectively.

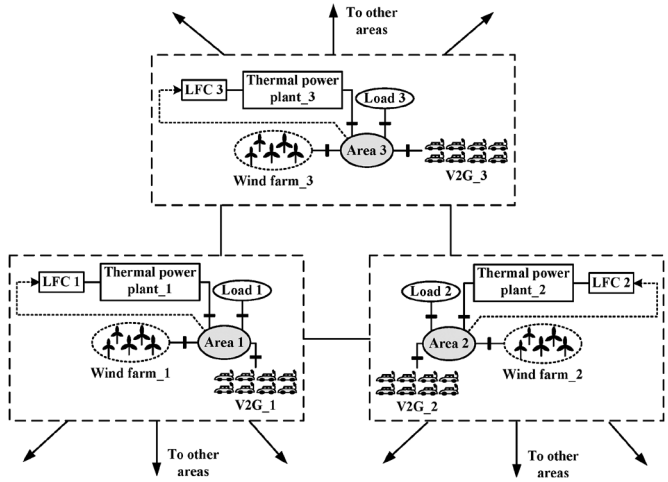

Fig. 1. A smart multi-area interconnected power system.

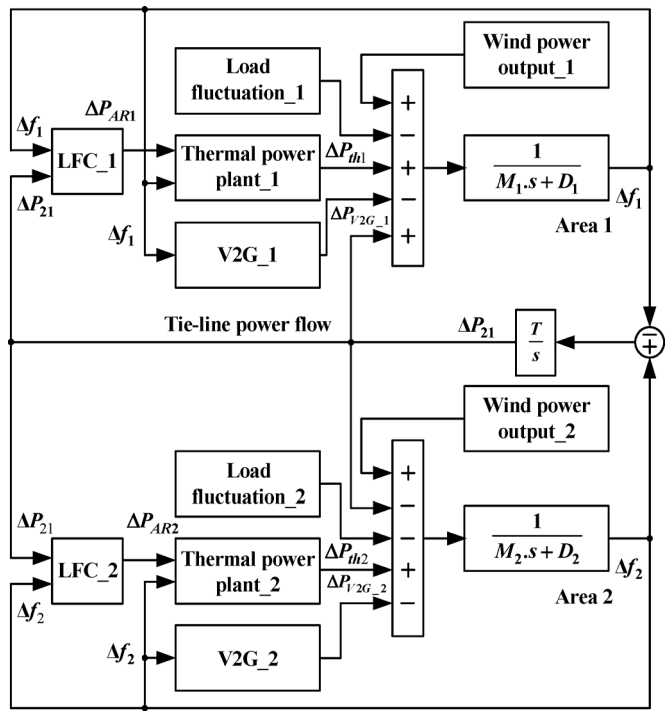

Fig. 2. Linearized model of the smart 2-area interconnected power system.

Due to the sudden power change from the intermittent wind power and the load fluctuation, the thermal generator may not compensate sufficiently the power because of its slow dynamic response [24]. The fast dynamic response of vehicle battery-based multiple PHEVs is greatly expected to compensate additionally the real power unbalance in the system when the LFC capacity is inadequate.

By taking the dynamic response into consideration, the PHEV is faster than the turbine and governor of thermal generator. Consequently, the operational tasks are assigned according to the response speed as follows. The PHEV is responsible for damping the peak value of frequency oscillation rapidly. Subsequently, the turbine and governor of thermal generator are utilized for eliminating the steady state error of frequency fluctuation. The linearized model of the smart 2-area interconnected power system is shown in Fig. 2.

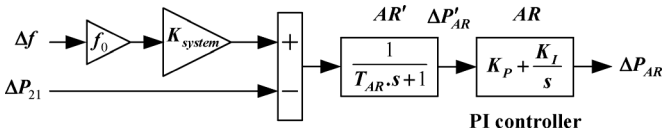

Fig. 3. LFC model.

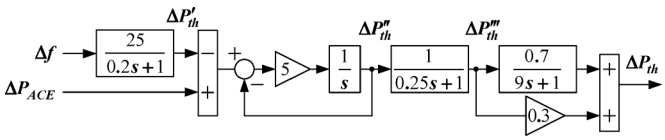

Fig. 4. Thermal power plant model.

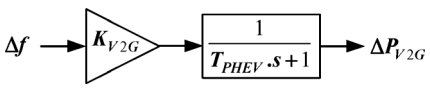

Fig. 5. V2G model.

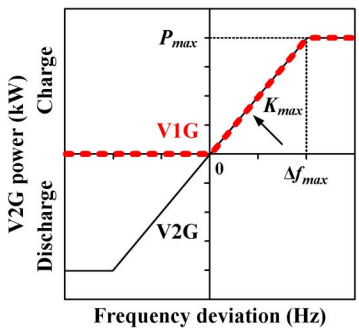

Fig. 6. V2G power control.

The models of LFC, thermal power plant, and V2G are shown in Figs. 3, 4, and –5, respectively. In the V2G model, the transfer function for calculation delay is approximately represented by the first-order transfer function with the time delay (T_{PHEV}). The parameters for system, battery model and V2G control [17] are provided in Appendix.

In Fig. 2, the linearized state equations can be expressed as follows:

$$\Delta \dot{X} = A\Delta X + B\Delta u \tag{1}$$

$$\Delta Y = C\Delta X + D\Delta u \tag{2}$$

$$PK_{area1}(s) = K_{P1} + \frac{K_{I1}}{s} \tag{3}$$

$$PK_{area2}(s) = K_{P2} + \frac{K_{I2}}{s} \tag{4}$$

where the state vector $\Delta X = [\Delta f_1\ \Delta P_{AR1}\ \Delta P'_{th1}\ \Delta P''_{th1}\ \Delta P'''_{th1}\ \Delta P_{th1}\ \Delta P_{V2G\_1}\ \Delta P_{21}\ \Delta f_2\ \Delta P_{AR2}\ \Delta P'_{th2}\ \Delta P''_{th2}\ \Delta P'''_{th2}\ \Delta P_{th2}\ \Delta P_{V2G\_2}]^T$. Δf_1 and ΔP_{AR1} are the changes of frequency and AR in area 1, respectively. $\Delta P'_{th1}$, $\Delta P''_{th1}$, $\Delta P'''_{th1}$ and ΔP_{th1} are the changes of output power of thermal power plant in area 1. ΔP_{V2G_1} is the change of V2G power in area 1. ΔP_{21} is the change of tie-line power flow from area 2 to area 1. Δf_2 and ΔP_{AR2} are the changes of frequency and AR in area 2, respectively. $\Delta P'_{th2}$, $\Delta P''_{th2}$, $\Delta P'''_{th2}$ and ΔP_{th2} are the changes of output power of thermal power plant in area 2. ΔP_{V2G_2} is the change of V2G power in area 2. The output vector $\Delta Y = [\Delta P'_{AR1}\ \Delta P'_{AR2}]^T$, the control output signal $\Delta u = [\Delta P_{AR1}\ \Delta P_{AR2}]^T$. $\Delta P'_{AR1}$ and $\Delta P'_{AR2}$ are the changes of the AR output signal in area 1 and area 2, respectively. PK_{area1} and PK_{area2} are the proposed robust PI controllers of LFC in area 1 and area 2, respectively. The system in (1) is a multi-input multi-output system and referred to as the nominal plant G.

III. V2G Power Control

In [17], the V2G power control can be described as follows.

A. V2G Power Control

As illustrated in Fig. 6, the V2G power output (P_{V2G}) can be controlled by the droop characteristics against the frequency deviation (Δf) as

$$P_{V2G} = \begin{cases} K_{V2G}\Delta f & (|K_{V2G}\Delta f| \le P_{max}) \\ P_{max} & (P_{max} < |K_{V2G}\Delta f|) \end{cases} \tag{5}$$

where K_{V2G} is the V2G gain tuned by taking a tradeoff between the V2G effect and the battery SOC deviation range into consideration. P_{max} is the maximum V2G power defined by the 200 V/25 A home outlet. Also, K_{V2G} can be computed by

$$K_{V2G} = K_{max}\left[1 - \left(\frac{\mathrm{SOC} - \mathrm{SOC}_{low(high)}}{\mathrm{SOC}_{max(min)} - \mathrm{SOC}_{low(high)}}\right)^n\right] \tag{6}$$

where SOC_{min}, SOC_{low}, SOC_{high}, SOC_{max} and n are the minimum battery SOC, low battery SOC, high battery SOC, maximum battery SOC, and design parameters, respectively. The SOC can be controlled by the SOC balance control. Next, the V1G power (P_{V1G}) is calculated by

$$P_{V1G} = \begin{cases} K_{max}\Delta f & (0 < K_{max}\Delta f \le P_{max}) \\ P_{max} & (P_{max} < K_{max}\Delta f) \\ 0 & (K_{max}\Delta f < 0) \end{cases} \tag{7}$$

where K_{max} is the maximum V2G gain. As mentioned in [16], the average length for driving a car in Japan is short. Almost all cars are parked and plugged in the power grid. Normally, the battery SOC will become full during few hours because of the short driving distance. Accordingly, it is supposed that the average driving distance of all PHEVs in both areas is no long and almost all PHEVs in each area are plugged in the utility grid. Besides, based on [17] considering the charging need of user for the future journey and the various battery operating conditions during the V2G and V1G modes, it is assumed that there is no V2G control in each area during the first 4 hours and the V2G mode in area 1 is changed to the V1G mode at $t = 18$ h for charging the power of PHEVs with full charge during estimated 3–4 hours for next trip. Also, there is no V1G mode in area 2. The PHEVs installed in area 2 are not plugged out during $t = 4 - 24$ h in order to study the effect of battery SOC balance control around 50% without the PHEVs power charging with full charge. As a result, the time scale of simulation test is expanded to 24 hours.

IV. Proposed Design Technique

The proposed design method is explained as follows:

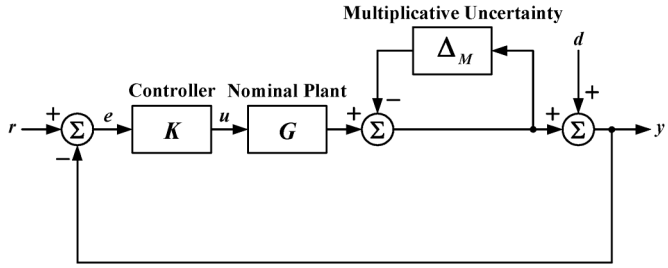

Fig. 7. Control system with inverse output multiplicative perturbation and external disturbance.

A. Fixed-Structure Mixed H_2/H_∞ Control Approach

To tune PI controllers of LFC in each area, the inverse output multiplicative perturbation is applied to model the system uncertainties [22]. The control system with inverse output multiplicative perturbation and external disturbance is shown in Fig. 7 where G is the nominal plant, K is the designed PI controller, $r(t)$ is the reference input, $e(t)$ is the error tracking, $d(t)$ is the external disturbance, $y(t)$ is the output of the system, and Δ_M is the unstructured system uncertainties such as various generating and loading conditions, variation of system parameters, etc. Note that Δ_M is formed by a multiplicative uncertainty. Based on the small gain theorem, for a stable multiplicative uncertainty, the system is stable if

$$\left\|\Delta_M(I+GK)^{-1}\right\|_\infty < 1 \tag{8}$$

then,

$$\left\|\Delta_M\right\|_\infty < 1 \Big/ \left\|(I+GK)^{-1}\right\|_\infty \tag{9}$$

The right hand side of (9) implies the size of system uncertainties or the robust stability margin against the system uncertainties. By minimizing $\|(I+GK)^{-1}\|_\infty$, the robust stability margin of the closed-loop system is maximum. This concept can be applied to design the robust controller as the cost function

$$J_\infty = \left\|(I+GK)^{-1}\right\|_\infty \tag{10}$$

In addition, the tracking error performance of the designed controller is also considered. The tracking error can be defined by the integral of the squared error as the cost function

$$J_2 = \int_0^\infty e^T(t)e(t)dt = \|E(s)\|_2^2 \tag{11}$$

where $e(t) = r(t) - y(t)$ is the error which can be obtained from the inverse laplace transformation of $E(s)$ with $\Delta_M = 0$ and $d(t) = 0$ as

$$E(s) = (I+GK)^{-1}R(s) \tag{12}$$

B. Battery SOC Deviation Control

Based on (5) and (6), P_{V2G} can be controlled by tuning the gain K_{V2G} against the frequency deviation. K_{V2G} can be adjusted by the SOC deviation control within the specified SOC range. Here, the initial SOC and target SOC in area 1 are set at 20% and 90%, respectively. Also, in area 2, the initial SOC and target SOC are set at 50% and 50%, respectively.

By taking the reach of the target SOC in area 1 and the initial and target SOC balancing in area 2 into account, the integral absolute error (IAE) values of the SOC deviation in area 1 ($\Delta\mathrm{SOC}_{area1}$) and area 2 ($\Delta\mathrm{SOC}_{area2}$) are applied in the design problem as follows:

$$\text{IAE of } \Delta\mathrm{SOC}_{area1} = \int_0^\infty |\Delta\mathrm{SOC}_{area1}|dt \tag{13}$$

$$\text{IAE of } \Delta\mathrm{SOC}_{area2} = \int_0^\infty |\Delta\mathrm{SOC}_{area2}|dt \tag{14}$$

From (13), the high IAE value of $\Delta\mathrm{SOC}_{area1}$ will give the rapid 90% target SOC arriving compared with the low IAE value of $\Delta\mathrm{SOC}_{area1}$. Also, in (14), the small IAE value of $\Delta\mathrm{SOC}_{area2}$ will provide the good performance of the 50% initial and target SOC balancing. The maximum IAE value of $\Delta\mathrm{SOC}_{area1}$ in (13) and the minimum IAE value of $\Delta\mathrm{SOC}_{area2}$ in (14) are highly expected in the optimization. Note that the inversion of the maximum IAE value of $\Delta\mathrm{SOC}_{area1}$ is the minimum IAE value of $\Delta\mathrm{SOC}_{area1}$.

As a result, the optimization problem can be formulated by

$$\text{Minimize } J_2 + J_\infty + 1 \Big/ \int_0^\infty |\Delta\mathrm{SOC}_{area1}|dt + \int_0^\infty |\Delta\mathrm{SOC}_{area2}|dt \tag{15}$$

Subject to

$$\begin{aligned} K_{P1-2,min} < K_{P1-2} < K_{P1-2,max} \\ K_{I1-2,min} < K_{I1-2} < K_{I1-2,max} \end{aligned} \tag{16}$$

where $K_{P1-2,min}$ and $K_{I1-2,min}$ are the minimum PI gains of LFC in area 1 and area 2, respectively. $K_{P1-2,max}$ and $K_{I1-2,max}$ are the maximum PI gains of LFC in area 1 and area 2, respectively. Note that the problem (15) is solved by the PSO [23].

Next, the enormous combination of PHEVs gives the high capability of V2G [14]. In [17], [18], the lumped V2G group-based large PHEVs can be controlled by the identically synchronized control of multiple PHEVs as the one controlled object for compensating the unbalanced power in the system. Here, the IAE values of $\Delta\mathrm{SOC}_{area1}$ and $\Delta\mathrm{SOC}_{area2}$ in (13), (14) are calculated based on each vehicle's SOC. Based on the SOC synchronization control among huge PHEVs in [17], [18], the IAE values of the SOC deviation in the case of multiple PHEVs can be computed approximately by multiplying the total number of PHEVs in each area with the IAE values of $\Delta\mathrm{SOC}_{area1}$ and $\Delta\mathrm{SOC}_{area2}$ in (13), (14) as follows:

$$\text{IAE of } \Delta\mathrm{SOC}_{area1} \text{ for multiple PHEVs} \approx N_{PHEV\_area1} \times \int_0^\infty |\Delta\mathrm{SOC}_{area1}|dt \tag{17}$$

$$\text{IAE of } \Delta\mathrm{SOC}_{area2} \text{ for multiple PHEVs} \approx N_{PHEV\_area2} \times \int_0^\infty |\Delta\mathrm{SOC}_{area2}|dt \tag{18}$$

where N_{PHEV_area1} and N_{PHEV_area2} are the total number of PHEVs in area 1 and area 2, respectively.

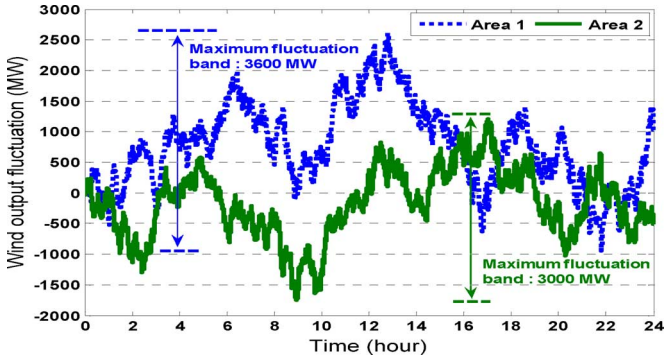

Fig. 8. Wind power output fluctuation.

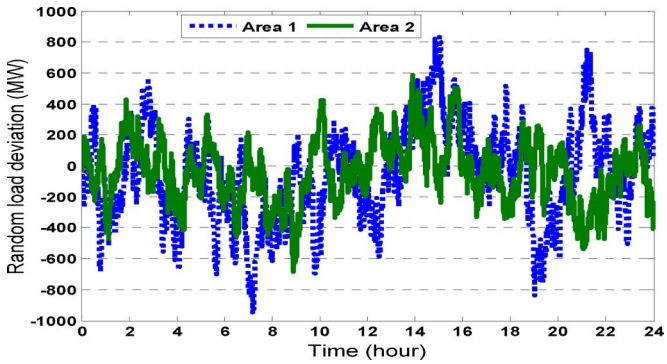

Fig. 9. Random load deviation.

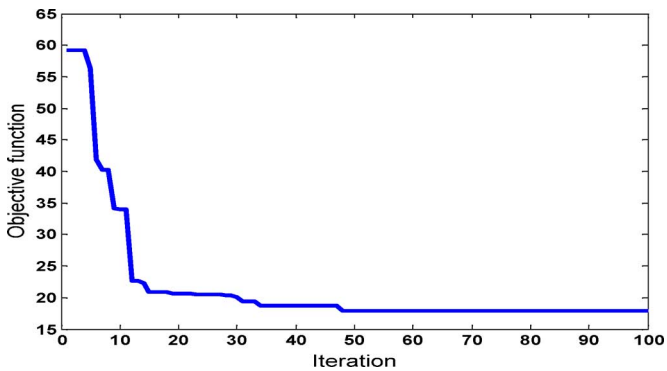

Fig. 10. Objective function versus iteration.

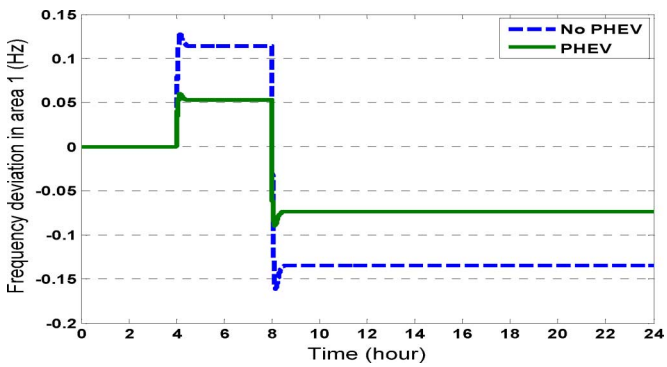

Fig. 11. Frequency deviation in area 1 under the step increases of wind power and load in the system model without governor and turbine.

V. Simulation Results

In this section, the searching parameters boundary and PSO parameters are set as follows: $K_{P1-2} \in [0.0001\ 5]$, $K_{I1-2} \in [0.0001\ 5]$, PSO sizes $= 50$, maximum iterations $= 100$, $c_1 = 2$, $c_2 = 2$, $w_{min} = 0.4$, and $w_{max} = 0.9$.

To optimize simultaneously the PI control parameters of LFC in both areas and the IAE values of $\Delta\mathrm{SOC}_{area1}$ and $\Delta\mathrm{SOC}_{area2}$, it is assumed that the wind power output fluctuation with the maximum deviation band in each area and the random load deviation in Figs. 8 and 9, respectively are subjected to the considered smart power system.

From (12), $R(s) = 1/(s+0.59)$ is selected instead of the step as the reference input to accomplish the H_2 norm value. As a result, the convergence curve of objective function is illustrated in Fig. 10. The proposed robust PI controllers of LFC in area 1 and area 2 (PK_{area1} and PK_{area2}) are

$$PK_{area1} = 2.1521 + \frac{0.0009}{s}, PK_{area2} = 2.4672 + \frac{0.0005}{s} \quad (19)$$

In the simulation study, the PK_{area1} and PK_{area2} cooperated with the proposed V2G control called "PLFC & PPHEV" is compared with the conventional PI controllers of LFC in area 1 and area 2 combined with the V2G control in [17], [18] denoted as "CLFC & CPHEV" and the conventional PI controllers of LFC in both area 1 and area 2 joined with the only V1G control based on (7) called "RLFC & RPHEV." Here, in the case of RLFC & RPHEV, the PI controller parameters of LFC in both areas are designed by minimizing the IAE values of the frequency deviation in area 1 (Δf_1) and area 2 (Δf_2) under the wind power output fluctuation and the random load deviation in Figs. 8, 9 as in the following objective function:

$$Minimize \int_0^\infty |\Delta f_1| dt + \int_0^\infty |\Delta f_2| dt \quad (20)$$

Subject to

$$K_{P1-2,min} < K_{P1-2} < K_{P1-2,max}$$
$$K_{I1-2,min} < K_{I1-2} < K_{I1-2,max} \quad (21)$$

In (20), the PI control parameters of LFC in area 1 and area 2 are automatically adjusted by the PSO under the same tuning parameters range of (15). After minimizing (20), the conventional PI controllers of LFC in area 1 and area 2 (RK_{area1} and RK_{area2}) are

$$RK_{area1} = 3.2186 + \frac{0.0061}{s}, RK_{area2} = 4.5621 + \frac{0.0069}{s} \quad (22)$$

To test the dynamic response of the PHEV and the thermal generator, it is assumed that the only 3000 MW step increase of wind power at $t = 4$ h in area 1 and the only 1500 MW step increase of load at $t = 8$ h in area 2 are subjected to the system model without and with governor and turbine, respectively. The frequency deviation under the step increases of wind power and load in the system model without governor and turbine is shown in Figs. 11 and 12, respectively.

As seen in Figs. 11 and 12, the peak values of frequency oscillation in area 1 and area 2 under the V2G control-based PHEVs can be highly suppressed in comparison with those of no PHEV. These demonstrate that the PHEV is used to damp swiftly the peak value of frequency fluctuation. Also, the frequency deviation under the step increases of wind power and load in the system model with governor and turbine is illustrated in Figs. 13 and 14, respectively.

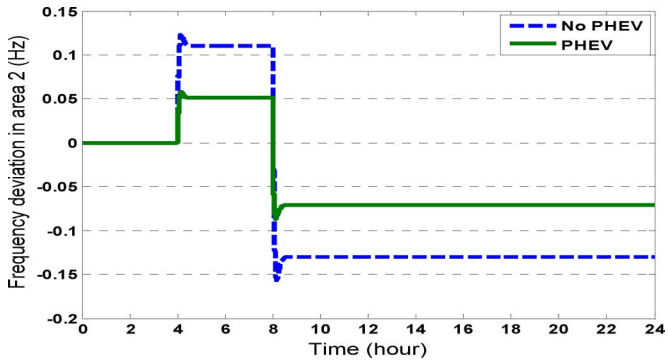

Fig. 12. Frequency deviation in area 2 under the step increases of wind power and load in the system model without governor and turbine.

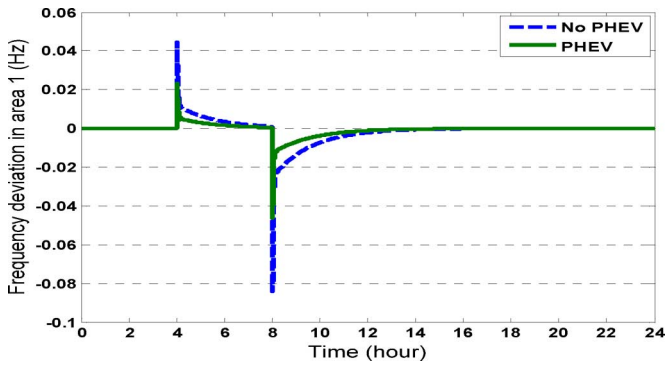

Fig. 13. Frequency deviation in area 1 under the step increases of wind power and load in the system model with governor and turbine.

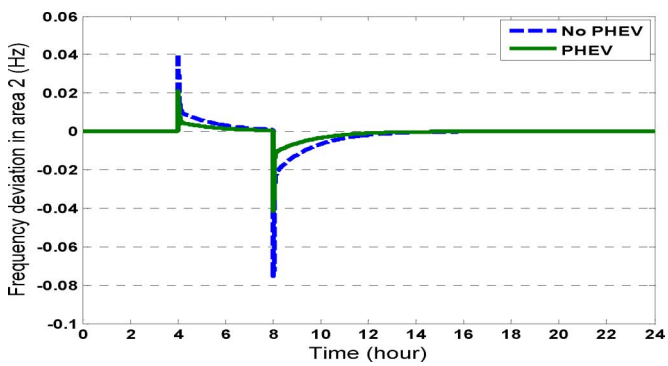

Fig. 14. Frequency deviation in area 2 under the step increases of wind power and load in the system model with governor and turbine.

With Figs. 13 and 14, the values of steady state error in the case of no PHEV and PHEV can be decreased to be zero. These show that the governor and turbine of thermal generator is utilized to manage the steady state error of frequency change. Consequently, the disturbances of wind power or load can be eliminated productively by the well coordinated control of the PHEV and the thermal generator.

In order to investigate the coordinated control of the V2G-based PHEVs and the LFC, the controls of only LFC, only V2G and LFC & V2G are applied to compensate the real power unbalance in the studied system separately. The frequency deviation in area 1 and area 2 under the only LFC, only V2G, and LFC & V2G controls is shown in Figs. 15 and 16, respectively.

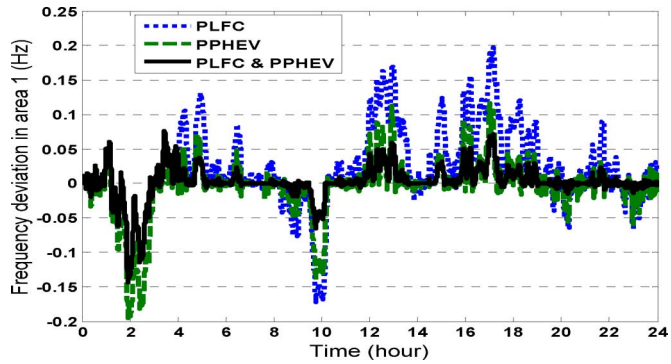

Fig. 15. Frequency deviation in area 1 under the controls of only LFC, only V2G, and LFC & V2G.

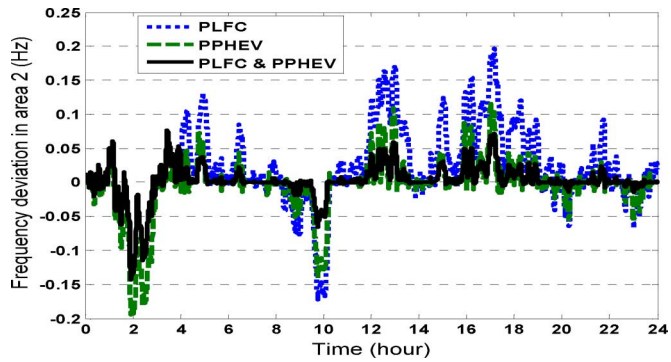

Fig. 16. Frequency deviation in area 2 under the controls of only LFC, only V2G, and LFC & V2G.

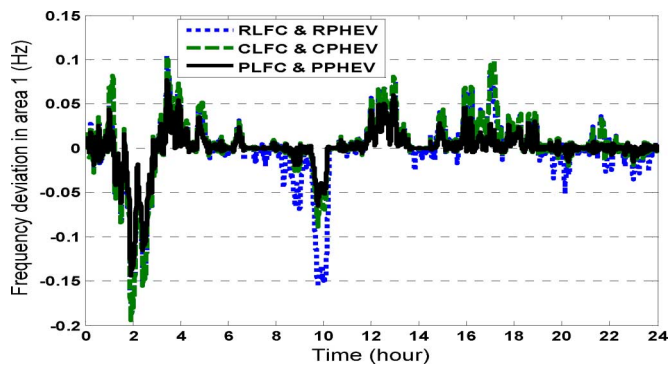

Fig. 17. Frequency deviation in area 1.

For Figs. 15 and 16, the PLFC & PPHEV can suppress capably the frequency oscillation in both area 1 and area 2 compared with those of the PLFC and the PPHEV. These indicate that the control of only LFC is greatly enhanced by the proposed V2G control.

In the normal case, the fluctuations of frequency and tie-line power flow are demonstrated in Figs. 17, 18, and 19, respectively.

The frequency and tie-line power flow deviations are greatly damped by the PLFC & PPHEVcompared with those of the CLFC & CPHEV and the RLFC & RPHEV. The fluctuations of frequency and tie-line power flow in the negative regions cannot be improved by the RLFC & RPHEV because there is no discharge mode. Also, the battery SOC and power outputs of V1G

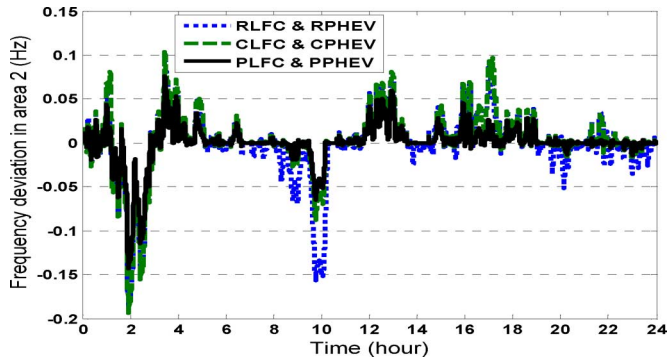

Fig. 18. Frequency deviation in area 2.

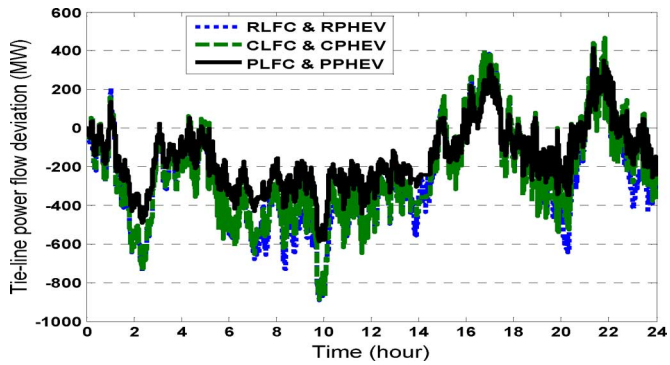

Fig. 19. Tie-line power flow deviation.

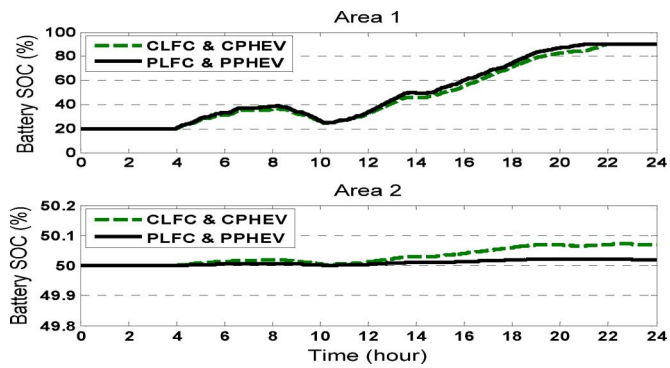

Fig. 20. Battery SOC in area 1 and area 2.

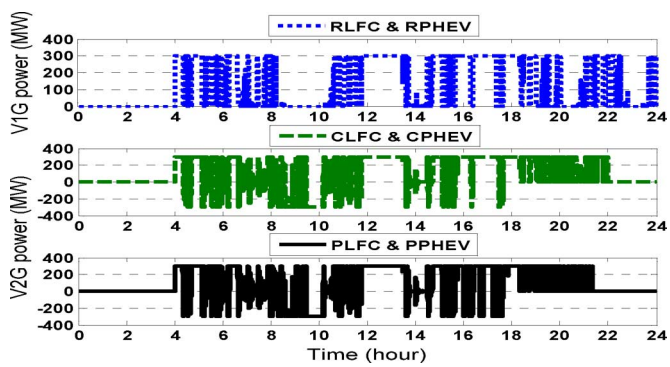

Fig. 21. V1G and V2G power outputs in area 1.

and V2G in area 1 and area 2 are shown in Figs. 20, 21, and –22, respectively.

In Fig. 20, the PLFC & PPHEV in area 1 can reach fast the 90% target SOC. Also, in area 2, the PLFC & PPHEV can

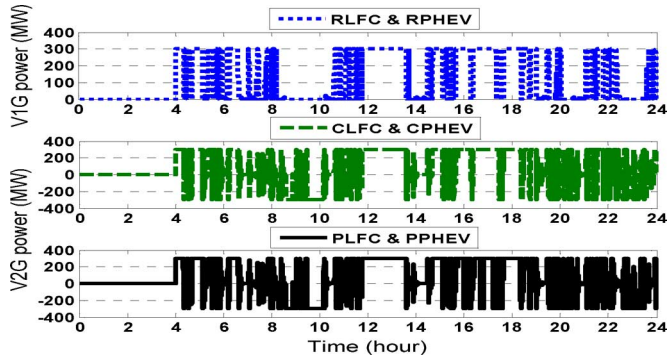

Fig. 22. V1G and V2G power outputs in area 2.

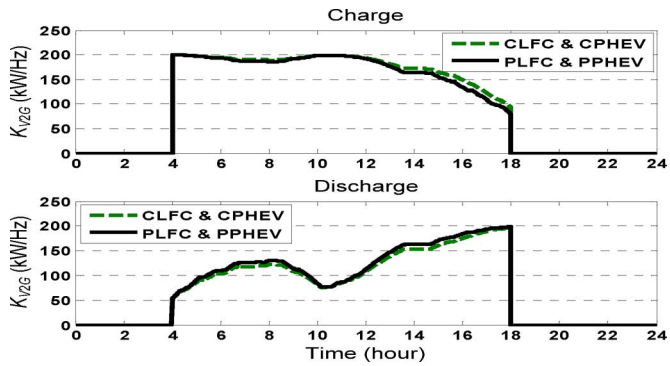

Fig. 23. V2G gains of charge and discharge in area 1.

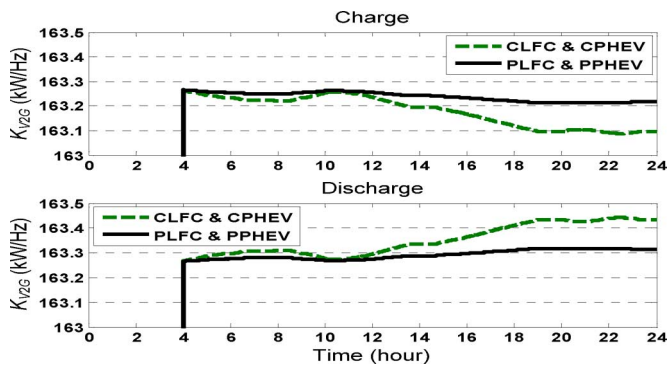

Fig. 24. V2G gains of charge and discharge in area 2.

suppress effectively the battery SOC around 50% in comparison with the CLFC & CPHEV. These result in the better V2G power control effects based on the proposed optimized battery SOC deviation control as exhibited in Figs. 21 and 22. Also, the RLFC & RPHEV can control satisfyingly the only V1G power charging in each area. Thus, the frequency and tie-line power flow oscillations in the positive zones can be alleviated as seen in Figs. 17, 18, and –19, respectively. The V2G gains of charge and discharge in area 1 and area 2 are demonstrated in Figs. 23 and 24, respectively. The proposed V2G gains for the charge and discharge in each area can be controlled efficiently in comparison to those of the conventional V2G gains. Note that the V2G mode in area 1 is switched to the V1G mode since $t = 18$ h.

To investigate the robustness of the PLFC & PPHEV against the system parameters change, the absolute maximum frequency deviation in area 1 and area 2 ($|\Delta f_1|_{max}$ and $|\Delta f_2|_{max}$) and the absolute maximum tie-line power flow deviation ($|\Delta P_{21}|_{max}$) are tested under the wind power output

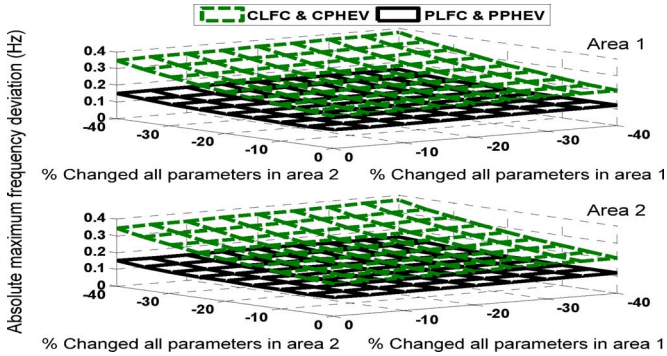

Fig. 25. Absolute maximum frequency deviation in area 1 and area 2.

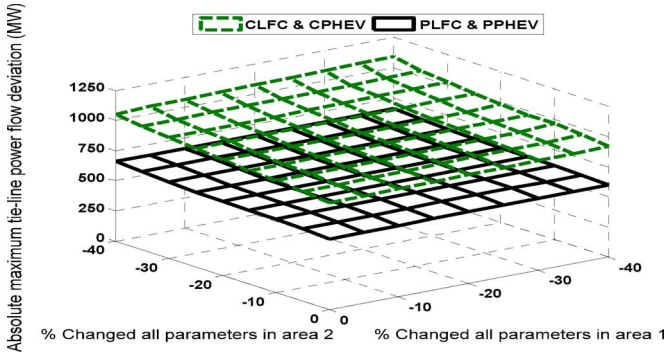

Fig. 26. Absolute maximum tie-line power flow deviation.

fluctuation and the random load deviation as shown in Figs. 8 and 9, respectively.

Figs. 25 and 26 demonstrate the values of $|\Delta f_1|_{max}$, $|\Delta f_2|_{max}$ and $|\Delta P_{21}|_{max}$ while all system parameters are decreased from 0% to -40% of the normal values in each area. The values of $|\Delta f_1|_{max}$, $|\Delta f_2|_{max}$ and $|\Delta P_{21}|_{max}$ in the case of CLFC & CPHEV increase highly when all system parameters decrease. On the contrary, the PLFC & PPHEV provides the greatly lower $|\Delta f_1|_{max}$, $|\Delta f_2|_{max}$ and $|\Delta P_{21}|_{max}$ values. These indicate that the PLFC & PPHEV is very robust to the system parameters variation.

In the case of changed system parameters, it is supposed that the considered system is operated under the wind power output fluctuation and the random load deviation in Figs. 8 and 9, respectively. During the simulation, it is assumed that the installed PHEVs in area 2 are decreased to as 30 000 from 60 000. This exhibits that the total V2G power capacity in area 2 is half reduced. In addition, it is supposed that the M_1 and M_2 are decreased by 40% from the normal values. Next, normally, the load damping coefficient can be changed from the positive damping to the negative damping when the considered system is operating at the unstable point. For example, in the extreme case of a heavily loaded generator operating on a long transmission link, it may result in the leading of negative damping to an oscillatory loss of stability [25]. Accordingly, it is assumed that the D_2 is changed from 2 (positive damping) to -0.9975 (negative damping) at $t = 19$ h. This implies that the studied area 2 is changed from the stable mode to the unstable mode at $t = 19$ h. Simulation results of the frequency deviation and tie-line power flow fluctuation are demonstrated in Figs. 27, 28, and –29, respectively.

The CLFC & CPHEV and the RLFC & RPHEV failto damp the frequency and tie-line power flow fluctuations totally. The

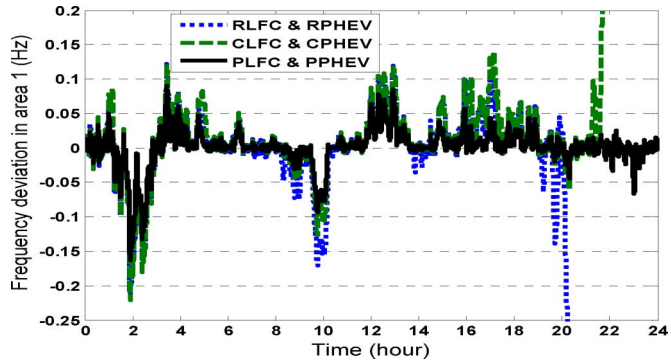

Fig. 27. Frequency deviation in area 1 (changed system parameters).

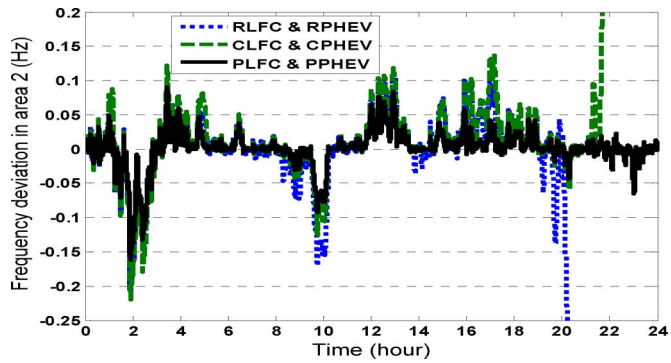

Fig. 28. Frequency deviation in area 2 (changed system parameters).

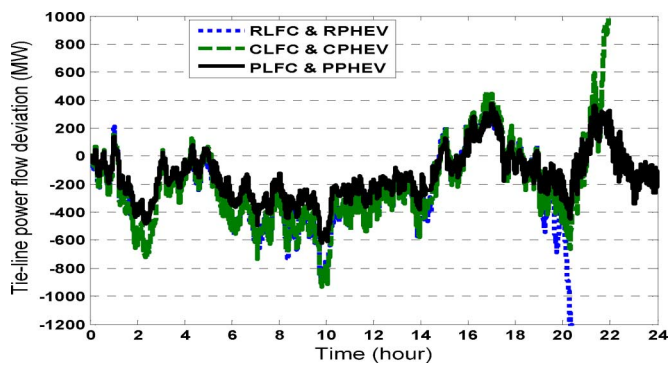

Fig. 29. Tie-line power flow deviation (changed system parameters).

system becomes unstable entirely. On the contrary, the PLFC & PPHEV can compensate the unbalanced real power in the interconnected power system productively.

Next, the battery SOC and power outputs of V1G and V2G in both areas under the system parameters change are illustrated in Figs. 30, 31, and –32, respectively.

In Fig. 30, the CLFC & CPHEV in area 1 reaches slowly the 90% target SOC. Besides, in area 2, the battery SOC of the CLFC & CPHEV is raised up. On the other hand, the PLFC & PPHEV is capable of controlling the battery SOC in both areas. With Figs. 31 and 32, the RLFC & RPHEV cannot control the V1G power outputs in each area during 20–24 h. In the case of CLFC & CPHEV, the V1G power charging in area 1 for the next trip is charged at the level of maximum power during 21.5–22 h. Also, the V2G power output in area 2 is charged at the maximum power level during 21.5–24 h because the system is performed in the unstable mode since $t = 21.5$ h. On the contrary, the PLFC & PPHEV can manage efficiently the V2G power outputs in each area. These results confirm the superior robustness and

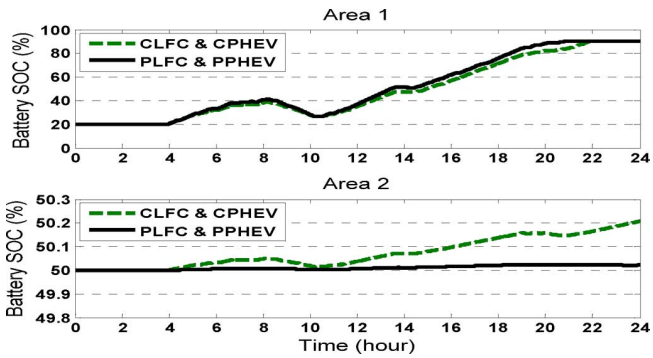

Fig. 30. Battery SOC in area 1 and area 2 (changed system parameters).

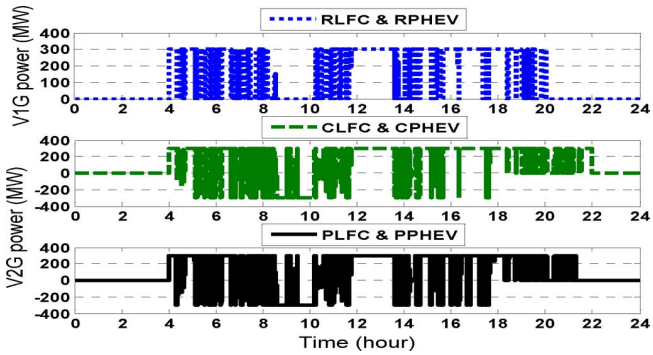

Fig. 31. V1G and V2G power outputs in area 1 (changed system parameters).

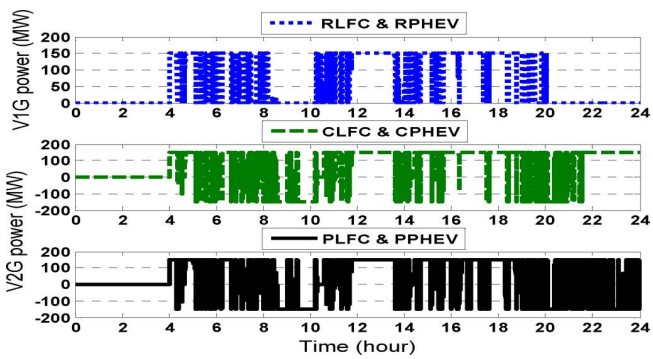

Fig. 32. V1G and V2G power outputs in area 2 (changed system parameters).

LFC control effects of the PLFC & PPHEV beyond the CLFC & CPHEV and the RLFC & RPHEV.

VI. Conclusions

The new coordinated V2G control and frequency controller for robust LFC in the smart grid system with wind power penetration has been presented in this paper. The V2G power output considering the proposed optimized battery SOC deviation control can be controlled effectively. The PSO based on the fixed-structure mixed H_2/H_∞ control technique is applied to tune the PI control parameters of LFC concurrently. Simulation results demonstrate the robustness and coordinated control effects of the proposed V2G control and PI controllers of LFC against the changed system parameters and various operating conditions.

Appendix A
System Parameters

TABLE I
System Parameters

Parameters	Area 1	Area 2
Load capacity (MW)	33090	7090
Rated thermal power output (MW)	24252	5560
Inertia constant (s)	8.58	9.02
Load damping coefficient (puMW/puHz)	2	2
Tie-line synchronizing power coefficient (s)	14	
Grid constant for AR calculation (puMW/puHz)	5	5
LFC capacity (MW)	±496	±106
LFC control approach	LFC	LFC
Time constant for frequency detection (s)	0.1	0.1
Time constant for AR calculation (s)	4	4
Communication delay from control center (s)	1	1

Appendix B
Battery Model

The battery SOC is updated as follows:

$$\frac{d\mathrm{SOC}}{dt} = \eta I \tag{B.1}$$

where η is the efficiency of charge and discharge. Also, the battery CCV (closed circuit voltage) is defined as follows:

$$CCV = V_{nom} + \alpha\frac{RT}{F}\ln\left[\frac{\mathrm{SOC}}{C_{nom} - \mathrm{SOC}}\right] + R_{\mathrm{int}} I \tag{B.2}$$

where R, F, T and R_{int} are the gas constant, faraday constant, battery temperature and internal resistance, respectively.

TABLE II
Battery Model Parameters

Parameters	Area 1	Area 2
Nominal voltage (V_{nom}) (V)	325.6	325.6
Nominal capacity (C_{nom}) (Ah)	50	50
Energy capacity (kWh)	16.28	16.28
Tuning parameter (α)	15	15
Efficiency of charge and discharge (η)	1	1
Internal resistance (R_{int}) (Ohm)	0.352	0.352

Appendix C
V2G Control Parameters

TABLE III
V2G Control Parameters

Parameters	Area 1	Area 2
Maximum V2G power (P_{max}) (kW)	5	5
Maximum V2G gain (K_{max}) (kW/Hz)	200	200
n, SOC_{min}, SOC_{low}, SOC_{high}, SOC_{max} (%)	2, 10, 20, 80, 90	
Initial SOC, target SOC (%)	20, 90	50, 50
Time to plug out (h)	18	-
Time for estimated V1G charging (h)	3-4	-
Delay time (T_{PHEV}) (s)	1	1
Number of PHEVs	60000	60000

REFERENCES

[1] M. E. Khodayar, L. Wu, and M. Shahidehpour, "Hourly coordination of electric vehicle operation and volatile wind power generation in SCUC," *IEEE Trans. Smart Grid*, vol. 3, no. 3, pp. 1271–1279, Sep. 2012.

[2] K. Moslehi and R. Kumar, "A reliability perspective of the smart grid," *IEEE Trans. Smart Grid*, vol. 1, no. 1, pp. 57–64, Jun. 2010.

[3] R. Podmore and M. R. Robinson, "The role of simulators for smart grid development," *IEEE Trans. Smart Grid*, vol. 1, no. 2, pp. 205–212, Sep. 2010.

[4] I. D. Margaris, S. A. Papathanassiou, N. D. Hatziargyriou, A. D. Hansen, and P. Sørensen, "Frequency control in autonomous power systems with high wind power penetration," *IEEE Trans. Sustainable Energy*, vol. 3, no. 2, pp. 189–199, Apr. 2012.

[5] Y. Ota, H. Taniguchi, T. Nakajima, K. M. Liyanage, K. Shimizu, T. Masuta, J. Baba, and A. Yokoyama, "Effect of autonomous distributed vehicle-to-grid (V2G) on power system frequency control," in *Proc. 2001 IEEE Ind. Inf. Syst. Conf.*, pp. 481–485.

[6] C. Pang, P. Dutta, and M. Kezunovic, "BEVs/PHEVs as dispersed energy storage for V2B uses in the smart grid," *IEEE Trans. Smart Grid*, vol. 3, no. 1, pp. 473–482, Mar. 2012.

[7] Z. Fan, "A distributed demand response algorithm and its application to PHEV charging in smart grids," *IEEE Trans. Smart Grid*, vol. 3, no. 3, pp. 1280–1290, Sep. 2012.

[8] E. Sortomme, M. M. Hindi, S. D. James MacPherson, and S. S. Venkata, "Coordinated charging of plug-in hybrid electric vehicles to minimize distribution system losses," *IEEE Trans. Smart Grid*, vol. 2, no. 1, pp. 198–205, Mar. 2011.

[9] W. Su and M.-Y. Chow, "Performance evaluation of an EDA-based large-scale plug-in hybrid electric vehicle charging algorithm," *IEEE Trans. Smart Grid*, vol. 3, no. 1, pp. 308–315, Mar. 2012.

[10] Y. Cao, S. Tang, C. Li, P. Zhang, Y. Tan, Z. Zhang, and J. Li, "An optimized EV charging model considering TOU price and SOC curve," *IEEE Trans. Smart Grid*, vol. 3, no. 1, pp. 388–393, Mar. 2012.

[11] A. Yokoyama, "Smarter grid I," *IEEJ J.*, vol. 30, no. 2, pp. 94–97, 2010.

[12] A. Yokoyama, "Smarter grid II," *IEEJ J.*, vol. 30, no. 3, pp. 163–167, 2010.

[13] M. Takagi, K. Yamaji, and H. Yamamoto, "Power system stabilization by charging power management of plug-in hybrid electric vehicles with LFC signal," in *Proc. 2009 IEEE Veh. Power Propulsion Conf.*, pp. 822–826.

[14] K. Shimizu, T. Masuta, Y. Ota, and A. Yokoyama, "Load frequency control in power system using vehicle-to-grid system considering the customer convenience of electric vehicles," in *Proc. 2010 IEEE Power Syst. Technol. Conf.*, pp. 1–8.

[15] Y. Ota, H. Taniguchi, T. Nakajima, K. M. Liyanage, and A. Yokoyama, "An autonomous distributed vehicle-to-grid control of grid-connected electric vehicle," in *Proc. 2009 IEEE Ind. Inf. Syst. Conf.*, pp. 414–418.

[16] T. Masuta and A. Yokoyama, "Supplementary load frequency control by use of a number of both electric vehicles and heat pump water heaters," *IEEE Trans. Smart Grid*, vol. 3, no. 3, pp. 1253–1262, Sep. 2012.

[17] Y. Ota, H. Taniguchi, T. Nakajima, K. M. Liyanage, J. Baba, and A. Yokoyama, "Autonomous distributed V2G (vehicle-to-grid) considering charging request and battery condition," in *Proc. 2010 IEEE Innov. Smart Grid Technol. Conf.*, pp. 1–6.

[18] Y. Ota, H. Taniguchi, T. Nakajima, K. M. Liyanage, J. Baba, and A. Yokoyama, "Autonomous distributed V2G (vehicle-to-grid) satisfying scheduled charging," *IEEE Trans. Smart Grid*, vol. 3, no. 1, pp. 559–564, Mar. 2012.

[19] P. P. Khargonekar and M. A. Rotea, "Mixed H_2/H_∞ control: A convex optimization approach," *IEEE Trans. Autom. Control*, vol. 36, no. 7, pp. 824–837, Jul. 1991.

[20] M. A. Rotea and P. P. Khargonekar, "H_2 optimal control with an H_∞ constraint: The state feedback case," *Automatica*, vol. 27, no. 2, pp. 307–316, Mar. 1991.

[21] B. T. Thanh and M. Parnichkun, "Balancing control of bicyrobo by particle swarm optimization-based structure-specified mixed H_2/H_∞ control," *Int. J. Adv. Robot. Syst.*, vol. 5, no. 4, pp. 395–402, 2008.

[22] D.-W. Gu, P. H. Petkov, and M. M. Konstantinov, *Robust Control Design With MATLAB*. New York: Springer, 2005.

[23] J. Kennedy and R. Eberhart, "Particle swarm optimization," in *Proc. 1995 IEEE Neural Netw. Conf.*, pp. 1942–1948.

[24] P. Kundur, *Power System Stability and Control*. New York: McGraw-Hill, 1993.

[25] J. Machowski, J. W. Bialek, and J. R. Bumby, *Power System Dynamics: Stability and Control*. Hoboken, NJ, USA: Wiley, 2008.

Sitthidet Vachirasricirikul received the B.Eng., M.Eng. and D.Eng. degrees in Electrical Engineering from King Mongkut's Institute of Technology Ladkrabang (KMITL), Bangkok, Thailand in 1997, 2003, and 2010, respectively. He is currently a lecturer of electrical engineering department, school of engineering at University of Phayao (UP), Phayao, Thailand. His research interests include power system stability, computational intelligence and robust control application to power system stabilization.

Issarachai Ngamroo received the B.Eng. degree in Electrical Engineering from KMITL, Bangkok, Thailand in 1992. He continued his education under the Monbusho Scholarship from the Japanese Government at Osaka University, where he earned his M.Eng. and Ph.D. degrees in Electrical Engineering in 1997 and 2000, respectively. Currently, he is an associate professor of electrical engineering department, faculty of engineering, KMITL. His research interests are in the areas of power system stability, dynamics, and control.